INTERNATIONAL JOURNAL FOR NUMERICAL METHODS IN FLUIDS
Int. J. Numer. Meth. Fluids 2000; **32**: 799–821

Upwinded finite difference schemes for dense snow avalanche modeling

G. Sartoris[a,*,1] and P. Bartelt[b,2]

[a] *Numerical Modeling GmbH, Alte Landstrasse 88,CH-8800 Thalwil, and Swiss Federal Institute of Technology, Institute for Structural Mechanics, CH-8093 Zürich, Switzerland*
[b] *Swiss Federal Institute for Snow and Avalanche Research, CH-7260 Davos Dorf, Switzerland*

SUMMARY

Avalanche dynamics models are used by engineers and land-use planners to predict the reach and destructive force of snow avalanches. These models compute the motion of the flowing granular core of dense snow avalanches from initiation to runout. The governing differential equations for the flow height and velocity can be approximated by a hyperbolic system of equations of first-order with respect to time, formally equivalent to the Euler equations of a one-dimensional isentropic gas. In avalanche practice these equations are presently solved analytically by making restrictive assumptions regarding mountain topography and avalanche flow behaviour. In this article the one-dimensional dense snow avalanche equations are numerically solved using the conservative variables and stable upwinded and total variation diminishing finite difference schemes. The numerical model is applied to simulate avalanche motion in general terrain. The proposed discretization schemes do not use artificial damping, an important requirement for the application of numerical models in practice. In addition, non-physical M-wave solutions are not encountered as in previous attempts to solve this problem using Eulerian finite difference methods and non-conservative variables. The simulation of both laboratory experiments and a field case study are presented to demonstrate the newly developed discretization schemes. Copyright © 2000 John Wiley & Sons, Ltd.

KEY WORDS: snow avalanche; hyperbolic equations; upwind; finite difference

1. INTRODUCTION

In alpine countries snow avalanche models are used by engineers and land-use planners to predict the reach and destructive force of snow avalanches. The most important application of these models is to prepare hazard maps, which divide endangered land into high- and low-risk zones. The models are also used to position and dimension avalanche defence structures, such

* Correspondence to: Zürcher Hochschule Winterthur, Postfach CH-8401, Winterthur, Switzerland.
[1] E-mail: guido.sartoris@zhwin.ch
[2] E-mail: bartelt@wsl.ch

Received October 1997
Revised April 1999

as dams, flow deflectors and highway snow sheds. The objective is to protect mountain communities from catastrophic avalanche events and prevent loss of life and property. For an overview of avalanche science, see Reference [1].

In practice, at present, simple models are employed. These models are based on the pointwise and piecewise analytical solution of the governing differential equations describing mass and momentum conservation respectively. In Switzerland these models have been calibrated over a long 30-year period by comparing actual measured avalanche runout distances with predicted model runout for extreme, that is, large, avalanche events, see References [2,3]. Consequently, the models are trustworthy engineering tools, especially in cases where the simplifying assumptions are valid. Sometimes however, analytical models are too restrictive in their assumptions regarding the avalanche path; they also require *a priori* assumptions regarding the avalanche flow behaviour. For example, analytical models divide the mountain terrain into three segments: the release zone, the avalanche track, and the runout zone — the last zone being defined as the region where the avalanche decelerates. Further, each segment has a constant slope angle, constant width and uniform flow. If these assumptions may be reasonable for large avalanche events [4], they are clearly questionable as they cannot model snow entrainment and deposition.

Numerical models [5–7] are now being proposed to replace the older analytical procedures. Numerical models can better approximate the mountain profile and more realistic flow laws that account for important physical processes. Despite these advantages, numerical methods for avalanche modelling are still in their infancy. Their employment in practice is difficult. Avalanche professionals are justifiably unwilling to employ numerical schemes containing many parameters, that have not been well calibrated. Because of the seriousness of their task, *protecting human life*, they prefer the older and simpler analytical models over perhaps better, but more uncertain, numerical models.

The purpose of this paper is to apply upwinded finite difference schemes to solve the quasi one-dimensional dense snow avalanche equations. The proposed model computes the flow height of the dense avalanche core and the flow velocity averaged over the flow height. The density of snow is assumed to be constant. We would like to show that numerical methods can be applied to model real avalanche events without the introduction of artificial dissipation. This is an important first step for using numerical models in practice. The goal is to provide engineers with a well-calibrated and stable numerical tool. The governing system of differential equations describing the avalanche flow contain only the well-calibrated coefficients specified in the Swiss Guidelines for Avalanche Runout Calculation [3].

In Section 2 we discuss the quasi one-dimensional snow avalanche problem together with the characterization of the governing equations. Sections 3 and 4 are devoted to the discretization of the governing equations. These equations are discretized in the conservative variables using a first-order upwind and a second-order total variation diminishing (TVD) difference scheme. In Section 5 the influence of the initial conditions and flow parameters on avalanche behaviour are studied. The simulation of a laboratory chute experiment and a real avalanche event are also presented. In Section 6 we state our conclusions.

2. PROBLEM FORMULATION

Dense snow avalanches contain a granular core of flowing snow. Flow velocities can be as high as 60 m/s and flow depths vary between one and several meters. The granules of the core vary in diameter depending on the physical state of the snowpack. Dry snow forms small particles; wet snow forms larger particles of several centimetres. Dry dense snow avalanches are often accompanied by a turbulent powder cloud; however, engineers are primarily interested in the destructive motion of the heavy granular core. For these reasons, the presented model is based on computing the flow height of the avalanche core which is assumed to be of constant density. The flow velocity is averaged over the flow height. For this model we present the governing equations and numerical results for the one-dimensional spatial case only. Extensions to include the second spatial dimension will be the subject of another work.

Let x be the horizontal co-ordinate, $Z(x)$ the mountain profile and $s(x)$ the length of the mountain profile, for example, starting from the top of the mountain. The formulation of our quasi one-dimensional modelling problem uses the variable s as the independent variable. In this model, an avalanche with a lateral width of $w(s)$ is described by two scalar fields $h(s)$ and $u(s)$. The first field, $h(s)$, represents the height of the snow at the point s and the second field, $u(s)$, gives the average over the snow height of the snow velocity tangential to the mountain profile at the point s. In this quasi one-dimensional model, the lateral flow width $w(s)$ of the avalanche is supposed to be known; in a future two-dimensional formulation this assumption will be dropped. Application of the principles of conservation of mass and momentum [8,9] lead to the following system of equations

$$\begin{cases} \dfrac{\partial(wh)}{\partial t} + \dfrac{\partial(whu)}{\partial s} = 0 \\ \dfrac{\partial(whu)}{\partial t} + \dfrac{\partial(whu^2)}{\partial s} = f - \dfrac{1}{2}\dfrac{\partial(\lambda w h^2)}{\partial s} \end{cases} \tag{1}$$

where f is the component of the force tangent to the mountain profile and $\lambda w(h^2/2)$ is an internal friction proportional to the hydrostatic pressure [10].

The λ parameter is given by

$$\begin{aligned} \lambda &= g\cos(\psi)\lambda_{\mathrm{a}} \quad \text{for } \frac{\partial u}{\partial s} > 0 \\ \lambda &= g\cos(\psi)\lambda_{\mathrm{p}} \quad \text{for } \frac{\partial u}{\partial s} \le 0 \end{aligned} \tag{2}$$

where ψ is the slope angle measured from the horizontal and g is the gravitational acceleration. This parameter splits into an *active* and *passive* part in order to account for the fact that unequal amounts of internal friction are introduced into the system, depending on whether the avalanche is being pulled apart (active case in the release zone) and/or if the avalanche is being compressed (passive case in the runout zone).

The active–passive internal friction is defined according to

$$\left.\begin{matrix}\lambda_a\\ \lambda_p\end{matrix}\right\} = \tan^2\left(45 \mp \frac{\phi}{2}\right) \tag{3}$$

The angle ϕ is termed the internal friction angle and is related to the angle of repose of snow. This formulation is based on chute experiments with flowing snow [11] and is adopted in the Swiss Guidelines. The Guidelines assume that $\phi \approx 25°$ leading to $1.5 \leq \lambda_p \leq 2.5$. An ideal fluid is often assumed for the active case, λ_a following [10,12].

In our model the force term f is approximated by [10]

$$f = \left[g \sin(\psi) - \text{sign}(u)\left(g\mu \cos(\psi) + \frac{gu^2}{\xi R}\right)\right] wh \tag{4}$$

The first term represents the gravitational acceleration tangent to the mountain slope. The second term is of phenomenological nature and models the flow friction. It contains two terms: a dry Coulomb-type sliding friction assumed to act at the base of the avalanche and a velocity dependent drag. The Coulomb-type friction is often expressed as

$$\mu = \tan \delta \tag{5}$$

The angle δ is termed the bed friction angle. For $\delta < \psi$ the avalanche will not come to rest. The turbulent friction parameter ξ is analogous to the Chezy coefficient in open channel flow hydraulics. The parameter R is the hydraulic radius; in the following we assume rectangular flow sections, i.e.

$$R = \frac{wh}{(w + 2h)} \tag{6}$$

Note that as flow heights decrease the turbulent friction term introduces more friction into the model since it is inversely proportional to h. The parameters μ and ξ are specified according to the Swiss Guidelines for Snow Avalanche Runout Calculation [3].

Let us rewrite the system (1) in matrix notation. In order to simplify the notation we first drop the identifier w so that h and λ will be defined as wh and λ/w. With the definition of the vector of the conservative variables $\vec{U} = (h, hu)^T$, the system (1) can be rewritten as follows

$$\frac{\partial \vec{U}}{\partial t} + \frac{\partial \vec{F}}{\partial s} = \vec{G} \text{ with } \vec{F} = \begin{pmatrix} hu \\ hu^2 + (\lambda/2)h^2 \end{pmatrix} \text{ and } \vec{G} = \begin{pmatrix} 0 \\ f \end{pmatrix} \tag{7}$$

This conservative formulation is best suited for the discretization of the governing equations since it leads to shock capturing discretization methods.

From the model (2), we obtain $\lambda = \lambda(s, \partial u/\partial s)$ with λ discontinuous with respect to $\partial u/\partial s$. In order for the derivatives of λ to exist in a classical sense, let $\bar{\lambda}$ be a smooth approximation of λ. We then have

$$\frac{1}{2}\frac{\partial}{\partial s}\bar{\lambda}wh^2 = \frac{\bar{\lambda}}{2}\frac{\partial}{\partial s}wh^2 + \frac{wh^2}{2}\frac{\partial \bar{\lambda}(s,z)}{\partial s} + \frac{wh^2}{2}\frac{\partial \bar{\lambda}(s,z)}{\partial z}\frac{\partial^2 u}{\partial s^2} \tag{8}$$

with $z = \partial u/\partial s$. Since $\lambda_b > \lambda_a$ we have $\partial\bar{\lambda}(s,z)/\partial z < 0$ so that the last term in (8) represents a dissipative term, but only in the neighborhood of a local extrema of u, otherwise the term is zero. In the present work such dissipative terms are neglected, therefore we can assume $\lambda = \lambda(s)$. Now, the term $(wh^2/2)(\partial\bar{\lambda}(s)/\partial s)$ in (8) does not depend on any partial derivatives of h or u and therefore it can be included inside the force term (4). In practice, if h is smaller than the mountain profile's curvature, this term can be neglected.

With these assumptions the system (7) is equivalent to

$$\frac{\partial \vec{U}}{\partial t} + A\frac{\partial \vec{U}}{\partial s} = \vec{G} \text{ with } A = \frac{\partial \vec{F}}{\partial U} = \begin{pmatrix} 0 & 1 \\ -u^2 + \lambda h & 2u \end{pmatrix} \tag{9}$$

This model, except for the right-hand-side vector $\vec{G}$, is the same as the Euler equations for a one-dimensional isentropic gas [8,13], or the one-dimensional shallow water equations on steep slopes without curvature [14]. The model consists of a hyperbolic system of equations of first-order.

The present work follows the general approach used when discretising the compressible Navier–Stokes equations of fluid dynamics where the hyperbolic part is separated and discretized independently from the viscous terms [8,15]. The assumption $\lambda = \lambda(s)$, crucial for the characterization of (9) as a hyperbolic system, corresponds in fact to the discretization of only the hyperbolic part of the governing equations. If considered necessary, the dissipative term in (8) may be discretized using central difference schemes [8,15].

When discretising the system (7) or (9), it is important to work with the conservative variables $\vec{U} = (h, hu)$ and not to change the formulation with respect to the non-conservative variables $\vec{U}^* = (h, u)$ as presented in Reference [9]. Although for this one-dimensional case a conservative form for the non-conservative variables $\vec{U}^*$ still exists

$$\frac{\partial \vec{U}^*}{\partial t} + \frac{\partial \vec{F}^*}{\partial s} = \vec{G}^* \text{ with } \vec{F}^* = \begin{pmatrix} hu \\ \lambda h + (u^2/2) \end{pmatrix} \text{ and } \vec{G}^* = \begin{pmatrix} 0 \\ f/h \end{pmatrix} \tag{10}$$

and for smooth solutions with $h \neq 0$ both formulations are equivalent, in practice, since $h = 0$ on large regions of the simulation domain, in particular ahead of the avalanche front, different solutions are obtained. The formulation with the non-conservative variables (10) leads to solutions with excessive accumulation of snow at the front of the avalanche. This may be seen by looking at the solutions of the Riemann problem characterized by the initial conditions

$$h(s, t=0) = \begin{cases} h_L & \text{if} \quad s < 0 \\ h_R & \text{if} \quad s \geq 0 \end{cases} \quad \text{and} \quad u(s, t=0) = \begin{cases} u_L & \text{if} \quad s < 0 \\ u_R & \text{if} \quad s \geq 0 \end{cases} \tag{11}$$

Let us consider the case $h_L \neq 0$, $u_L > 0$, $h_R = 0$, $u_R = 0$ with a small value for λ. With the additional assumptions $\vec{G} = 0$ and $\lambda = \text{const}$ the Riemann solution for both the hyperbolic systems (9) and (10) are known [16,17] and given by

$$(h, u) = \begin{cases} (h_L, u_L): y \leq c_0 \\ \left(\frac{1}{2}\left(\alpha - \frac{y}{3}\right)^2, \frac{2}{3}y + \alpha\right): c_0 \leq y < c_1 \\ (0, 0): c_1 \leq y \end{cases} \tag{12}$$

$$(h, u) = \begin{cases} (h_L, u_L): y \leq c_0 \\ (h_1, u_1): c_0 \leq y < c_1 \\ (0, 0): c_1 \leq y \end{cases} \tag{13}$$

where $y = s/t$. These solutions are displayed in Figure 1. For the first solution, the continuity conditions of $h(y)$ at $y = c_0$ and $y = c_1$ and of $u(y)$ at $y = c_0$ yield the values $c_0 = u_L - \sqrt{\lambda h_L}$, $c_1 = 3u_L - 2c_0$ and $\alpha = y_1/3$. No continuity requirement for $u(c_1)$ is necessary since we have $h(c_1) = 0$. For the second solution, the value of the four parameters c_0, c_1, h_1, u_1 are determined by imposing the Rankine–Hugoniot conditions at $y = c_0$ and $y = c_1$. The resulting non-linear equations are then solved numerically.

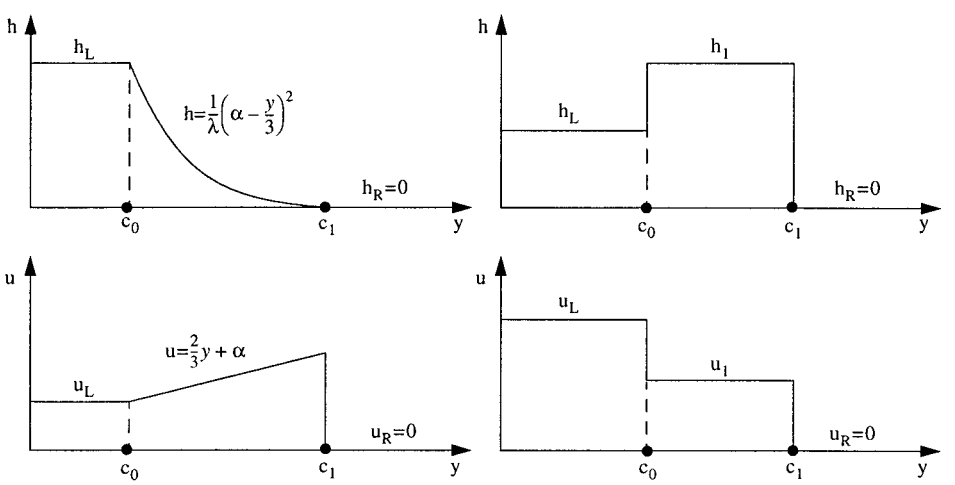

Figure 1. Riemann solutions for the hyperbolic system (9) and (10) and the initial conditions $h_R = u_R = 0$ and $u_L > 0$.

For the system with the conservative variables no shock wave can form at the avalanche's front as a consequence of the impossibility of fulfilling the Rankine–Hugoniot conditions when $h_R = 0$. Here, an expansion front is generated by the hydrostatic pressure. For the non-conservative variables, the value of λ is too small to create an expansion front and a shock front builds up. In this case the avalanche front is non-physically held back, a result of the non-conservative formulation. As an example, in the limit $\lambda \to 0$ the continuity equation for the velocity in (10) is decoupled from the continuity equations for the mass conservation and reduces to the Burger's equation [8]. In this case, the avalanche front moves with velocity $u_L/2$, but since the snow moves behind the front with velocity u_L, snow inevitably accumulates at the front. For this example, the formulation with the conservative variables gives the correct physical solution of a rectangular snow profile moving to the right with velocity u_L, without changing its shape.

Another example of unphysical solutions obtained if one uses the non-conservative variables is given by considering the M-wave solutions of Savage and Hutter [9]. These solutions, having an M-shape with a peak at each side and a trough in the middle, cannot be solutions of (9) because of the impossibility of fulfilling the Rankine–Hugoniot conditions on the edges.

3. FIRST-ORDER UPWINDED SCHEMES

Several algorithms are available to discretize the hyperbolic system (9); the most popular methods being finite difference methods. A survey and good introduction to this subject is given in Reference [8].

Difference schemes in the family of the space-centered Lax–Wendroff schemes have not been considered here. For these schemes the addition of an artificial damping term is an often required procedure in order to damp oscillations arising around steep gradients [8,9]. Instead, we have opted for a first-order upwinded Roe scheme and its extension to a second-order TVD scheme after the method of Harten [18].

At first, we present the discretization of the system (9) with a first-order upwinded scheme. The starting point is the discretization of the scalar hyperbolic equation

$$\frac{\partial u}{\partial t} + \frac{\partial f(u)}{\partial s} = 0 \text{ with } s \in \mathbb{R} \tag{14}$$

Let us use a regular grid in space $s_i = i\Delta s$ and in time $t = n\Delta t$. For a conservative explicit first-order scheme in space and time the general discretized form is

$$u_i^{n+1} = u_i^n - \sigma[f^*(u_i^n, u_{i+1}^n) - f^*(u_{i-1}^n, u_i^n)] \text{ with } \sigma = \frac{\Delta t}{\Delta s} \tag{15}$$

The scheme of Roe uses the flux function

$$f^*(u_i, u_{i+1}) = \frac{1}{2}\{f(u_i) + f(u_{i+1}) - |\lambda_{i+1/2}|(u_{i+1} - u_i)\} \tag{16}$$

with

$$\lambda_{i+1/2} = \begin{cases} \dfrac{f(u_{i+1}) - f(u_i)}{u_{i+1} - u_i} & \text{if } u_i \neq u_{i+1} \\ a(u_i) & \text{if } u_i = u_{i+1} \end{cases} \tag{17}$$

In the linear case, when $f = au$, this consistent scheme is stable and therefore convergent under the Courant–Friedrich–Lewy (CFL) condition $|a|\sigma < 1$. This condition is only necessary for the general non-linear case, the convergence of the finite difference solution is briefly presented in Reference [18].

The Roe scheme (16) for the hyperbolic scalar equations can be generalized to a hyperbolic system of equations if applied singularly to the characteristic variables. If the system (9) is strongly hyperbolic, a complete set of eigenvectors is available that diagonalizes the matrix A. Let S be the matrix in which the columns are the eigenvectors of A, i.e. $S^{-1}AS = \Lambda$ with Λ the diagonal matrix of eigenvalues. The characteristic variables $\vec{w}$ are defined by $\delta\vec{w} = S^{-1}\delta\vec{U}$ where δ stands for $\partial/\partial t$ or $\partial/\partial s$. With respect to these variables, the system is now decoupled

$$S^{-1}\frac{\partial \vec{U}}{\partial t} + \Lambda S^{-1}\frac{\partial \vec{U}}{\partial s} = S^{-1}\vec{G} \tag{18}$$

The system matrix A of Equation (9) has the eigenvalues $e_{\pm} = u \pm \sqrt{\lambda h}$ and eigenvectors $(1, e_{\pm})^T$; therefore the following matrices are obtained

$$\Lambda = \mathrm{diag}(e_+, e_-), \quad S = \begin{pmatrix} 1 & 1 \\ e_+ & e_- \end{pmatrix}, \quad S^{-1} = \frac{1}{2\sqrt{\lambda h}}\begin{pmatrix} -e_- & 1 \\ e_+ & -1 \end{pmatrix} \tag{19}$$

The vector formulation of the scalar first-order difference scheme (15) is

$$\vec{U}_i^{n+1} = \vec{U}_i^n - \sigma[\vec{F}^*(\vec{U}_i^n, \vec{U}_{i+1}^n) - \vec{F}^*(\vec{U}_{i-1}^n, \vec{U}_i^n)] \tag{20}$$

For the hyperbolic system (9), the Roe's scalar scheme is now applied to each decoupled equation (18), thus obtaining the difference scheme

$$\vec{F}^*(\vec{U}_i, \vec{U}_{i+1}) = \frac{1}{2}\{\vec{F}(\vec{U}_i) + \vec{F}(\vec{U}_{i+1}) - S_{i+1/2}|\Lambda_{i+1/2}|S^{-1}_{i+1/2}(\vec{U}_{i+1} - \vec{U}_i)\} \tag{21}$$

with $A_{i+1/2} = S_{i+1/2}\Lambda_{i+1/2}S^{-1}_{i+1/2}$. The matrix $A_{i+1/2} = \bar{A}(\vec{U}_i, \vec{U}_{i+1})$ is defined as any possible symmetric average of the form

$$\bar{A}(\vec{U}_1, \vec{U}_2) = \bar{A}(\vec{U}_2, \vec{U}_1) \quad \text{and} \quad \bar{A}(\vec{U}_1, \vec{U}_1) = A(\vec{U}_1) \tag{22}$$

It is common practice to use $\bar{A}(\vec{U}_1, \vec{U}_1) = A(\bar{h}, \bar{u})$ with $\bar{h}, \bar{u}$ given by an arithmetic average or the Roe's average

$$\bar{h} = \frac{h_1 + h_2}{2}, \quad \bar{u} = \frac{\sqrt{h_1}u_1 + \sqrt{h_2}u_2}{\sqrt{h_1} + \sqrt{h_2}} \tag{23}$$

4. SECOND-ORDER TVD SCHEMES

The first-order upwinded schemes presented previously for the scalar equation (14) are stable in the sense that they share the same properties of the weak solution. No new local extremas in s are created, the value of a local minimum is non-decreasing, the value of a local maximum is non-increasing and the total variation in s is non-increasing.

First-order upwinded schemes can be extended to second-order schemes in space with the general MUSCL procedure described in Reference [8]. However, these linear second-order schemes lack the above stability properties. The idea behind high resolution TVD schemes is to develop non-linear higher order schemes with similar stability properties as the first-order scalar schemes. As introduced by Harten [18,19], TVD difference schemes are devised so as not to increase the total variation of the numerical solution.

Scalar TVD schemes developed for the scalar hyperbolic equations are then applied as before to a hyperbolic system singularly to the characteristic variables. The following second-order TVD scheme has been presented by Harten [18,19] as an extension of Roe's first-order scheme for the discretization of a hyperbolic system. The flux function (21) is modified as follows

$$\vec{F}^*(\vec{U}_i, \vec{U}_{i+1}) = \frac{1}{2}\{\vec{F}(\vec{U}_i) + \vec{F}(\vec{U}_{i+1}) - S_{i+1/2}[G_{i+1/2} + |\Lambda_{i+1/2}|S^{-1}_{i+1/2}(\vec{U}_{i+1} - \vec{U}_i)]\} \tag{24}$$

where $G_{i+1/2} = \mathrm{diag}(G^1_{i+1/2}, G^2_{i+1/2})$ is a diagonal matrix with coefficients $k = 1, 2$

$$\begin{aligned} G^k_{i+1/2} &= S^k \max[0, \min(S^k g^k_{i-1/2}, S^k g^k_{i+1/2}, S^k g^k_{i+3/2})] \\ S^k &= \mathrm{sign}(g^k_{i+1/2}) \\ g_{i+1/2} &= |\Lambda_{i+1/2}|(1 - \sigma|\Lambda_{i+1/2}|)S^{-1}_{i+1/2}(\vec{U}_{i+1} - \vec{U}_i) \end{aligned} \tag{25}$$

Many other higher order TVD schemes have been presented [8,20]. They generally differ in the choice of the limiters chosen to make the second-order scheme a TVD scheme. More recently ENO schemes (essentially non-oscillatory) have been presented [21,22] as an extension to TVD schemes with the property that they preserve the second-order accuracy at local extremas. We do not consider these schemes to represent a real improvement to TVD schemes for the avalanche problem, since in general we are looking for smooth solutions.

In Figures 2 and 3 we compare the numerical solutions for the second-order scheme of Harten with two exact solutions of the Riemann problem (11) with $\vec{G} = 0$ and $\lambda = const$. In the first case we consider the Riemann solution (12). Since $h_R = 0$, a shock wave cannot build up

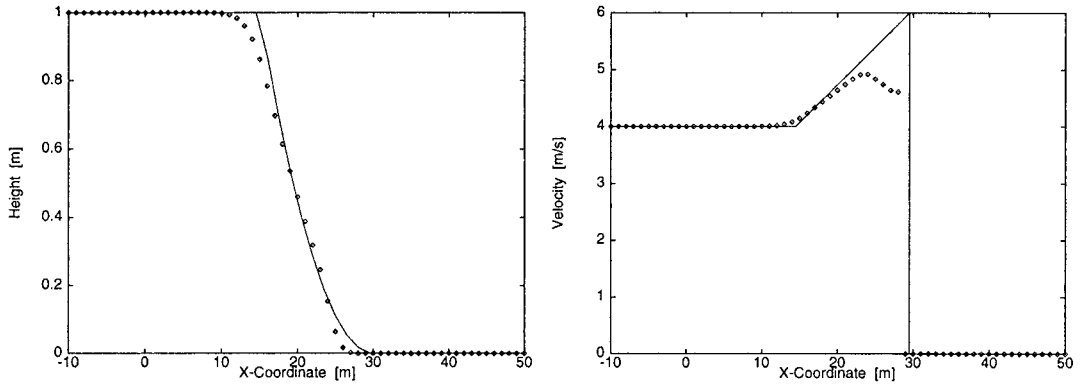

Figure 2. The Riemann solution at $t = 5$ s for Roe's second-order scheme and $h_L = 1m$, $u_L = 4$ m/s, $h_R = u_R = 0$, $\lambda = 20$ m/s^2.

at the avalanche's front and the hydrostatic pressure generates an expansion front. In the second case we release the restriction $h_R = 0$. Here a shock wave builds up at the front; however, the hydrostatic pressure is large enough to create an expansion wave behind the shock wave.

As a last numerical test, we compare the parabolic cap solution of [9] for a constant acceleration $a = 5$ m/s^2 and constant λ with the numerical solution, see Figure 4. The solution which solves both systems (9) and (10) is given by

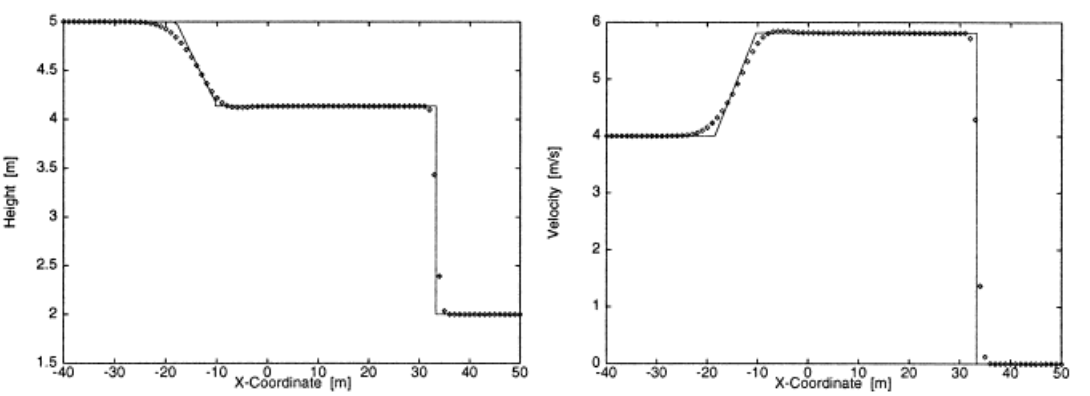

Figure 3. The Riemann solution at $t = 3$ s for Harten's second-order scheme and $h_L = 5m$, $u_L = 4$ m/s, $h_R = 2$ m, $u_R = 0$, $\lambda = 20$ m/s^2.

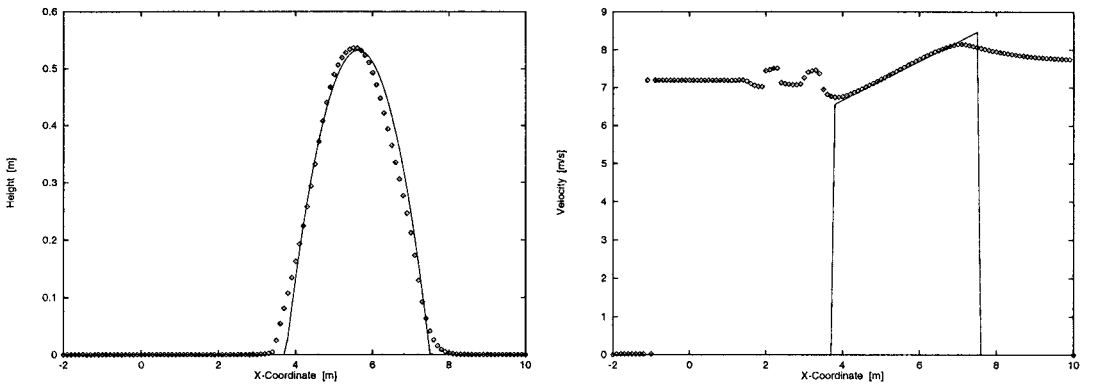

Figure 4. The cap solution of Reference [9] at $t = 1.5$ s for Harten's second-order scheme and $K = 1$, $\vec{G} = (0, h \times 5\ \mathrm{m/s^2})^T$.

$$(h(s,t), u(s,t)) = \begin{cases} (K\tilde{g}(t)^{-1}(1-\eta^2),\ at\ +\eta\sqrt{2K(1-\tilde{g}(t)^{-1})}) & \text{for } -1 < \eta < 1 \\ (0,0) & \text{for } |\eta > 1| \end{cases} \tag{26}$$

with $\eta = \tilde{g}(t)^{-1}(s - a(t^2/2))$, $K = 3/2\lambda M$, $M = \int h(s, t=0)\,\mathrm{d}s$ the total snow mass and $\tilde{g}(t)$ given by solving the equation

$$\sqrt{\tilde{g}(\tilde{g}-1)} + \log(\sqrt{\tilde{g}} + \sqrt{\tilde{g}-1}) = \sqrt{2K}\,t \tag{27}$$

We end this section with some remarks regarding the implementation. On large regions of the simulation domain, it is possible to have no snow at all. In this case, since $h = 0$ the system (9) is not strongly hyperbolic and the spectral decomposition (19) breaks down. However, if during the computation of the flux $\vec{F}(\vec{U}_1, \vec{U}_2)$ the averaged height $\bar{h} = (h_1 + h_2)/2$ is zero, by passing to the limit we have $\vec{F}(\vec{U}_1, \vec{U}_2) = 0$ and therefore the flux computation is unnecessary.

For small values of $\bar{h}$ numerical cancellation may strongly affect the computation of the flux. In order to avoid unstable behaviour, we have introduced a cut-off for the h field. As soon as we have $h < 10^{-10}$ m we set $h = 0$. This procedure has the drawback that the conservation laws for mass and momentum are not exactly fulfilled. However, it has the advantage that since the field h is now exactly zero, the flux afterwards is not computed, thus resulting in a large computational speed-up. In all computations the mass errors are extremely small.

5. SIMULATIONS

Previous numerical solutions employed the non-conservative formulation and both the Eulerian and Lagrangian finite difference schemes [9]. The Eulerian scheme used MacCormack's two-step explicit finite difference integration with an artificial viscosity. The equations were not

formulated with respect to the conservative variables. This method was eventually discarded because M-wave flow forms evolve, regardless of the shape of the initial mass configuration. As discussed in Section 2, the evolution of steep edges at the avalanche front is to be connected with the employment of the non-conservative formulation (10).

In a first series of numerical tests a problem similar to the one presented in Reference [9] is solved. Different initial mass configurations were released from rest down a straight $\psi = 32°$ incline. The width of the incline is 0.1 m and constant. In accordance with [9] the bed friction angle was chosen to be $\delta = 22°$; no viscous friction was specified, i.e. $1/\xi = 0$.

Figure 5 shows the development of a 0.1 m high 1.0 m long block-shaped mass. The internal angle of friction is $\phi = 29°$. The rectangular form was investigated because the steep edges of the initial form often produce numerical instabilities immediately after release. In addition, if spurious M-wave flow forms evolve they should be quickly apparent since the initial form is already very near to the M-wave shape.

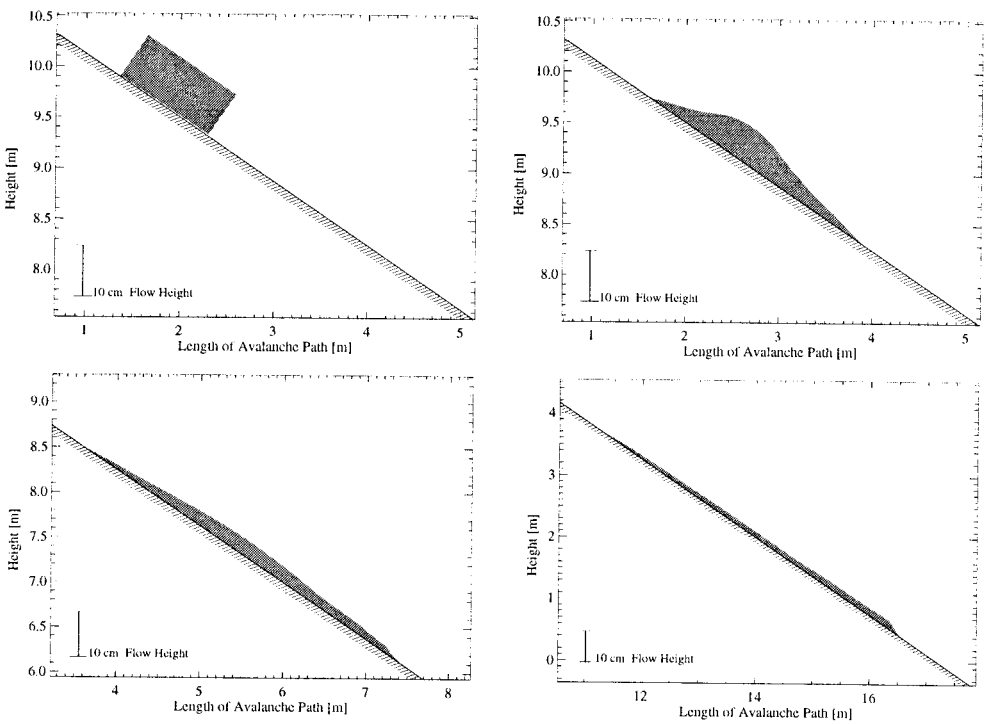

Figure 5. Top left: a rectangular-shaped mass ($h_0 = 0.1$ m) is released from rest down a straight $\psi = 32°$ incline. Note the steepness of the sides. Top right: the mass 0.4 s after release. Bottom left: The mass 2.5 s after release. The form is almost parabolic. Bottom right: the mass 4.0 s after release flowing in a wedge shape. The mass continues to flow in this form. Friction parameters: $\phi = 29°$, $\delta = 22°$, no viscous damping. The flow heights are increased by a factor of 5.

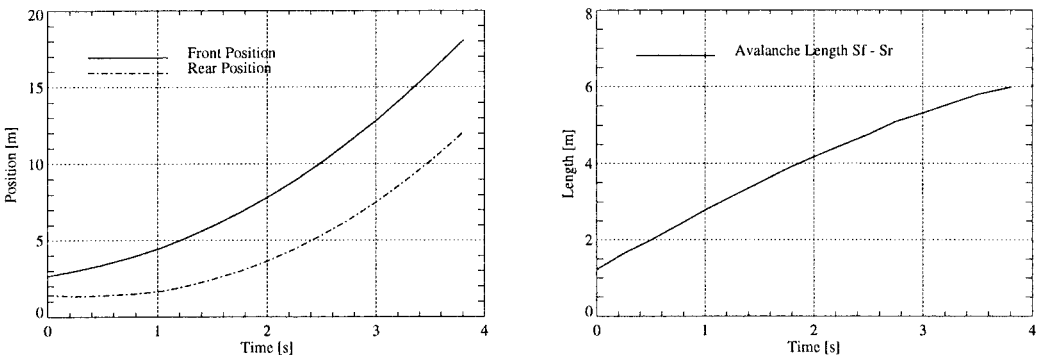

Figure 6. Left: position of front and rear of avalanche over time. Right: avalanche length over time. Friction parameters: $\phi = 29°$, $\delta = 22°$, no viscous damping.

Shortly after release the front spreads forward quickly and the flowing mass assumes a parabolic form. The rear of the avalanche remains almost stationary; it moves a little up the incline. Several seconds after release, the avalanche spreads out further. The avalanche front is steeper than the tail; however, the M-wave shape has not developed. The maximum flow heights are located well within the body of the avalanche. Four seconds after release the avalanche assumes its final flow form: a long wedge shape where the front flow heights are larger at the front. The flow heights decrease linearly towards the tail. In Figure 6 the position of the avalanche front s_f and rear s_r over time are plotted. The increase in avalanche flow length is almost linear. Note that the position of the rear is defined according to a specified flow height cut-off value. The tail of the avalanche was defined as occurring when the flow heights were smaller than 1 mm. The presented results are sensitive to this cut-off value.

In the next series of simulations a skewed parabolic shape was investigated. Different internal angles of friction were specified ($\phi = 0°$, 25° and 45°). The slope angle and the bed friction angle remained the same as before, $\psi = 32°$ and $\delta = 22°$ respectively. The initial pile shape and the different avalanche forms are shown in Figure 7.

Figure 7 shows that avalanche flow length increases with decreasing internal friction angle ϕ. Correspondingly, flow heights increase with increasing ϕ. Thus, the internal friction angle determines the longitudinal rigidity of the flow mass. For $\phi = 0°$ a short parabolic-shaped front forms. For higher ϕ values the parabolic front elongates and flatter fronts are predicted. Note that the avalanche of Figure 5 was calculated with nearly the same friction values as the bottom left avalanche of Figure 7. The flow forms should therefore be nearly the same. This is not the case; the maximum flow heights of the second avalanche are located near to the front. Since only the shape of the initial mass configurations differed, we conclude that the slight oscillations that develop on the top flow surface are a residue of the initial skewed parabolic pile geometry.

Figure 8 shows the position of the avalanche front and length of the avalanche over time for the different ϕ values. The influence of ϕ on the front position is not as strong as the influence on flow length. A near linear increase in flow length is predicted for all cases.

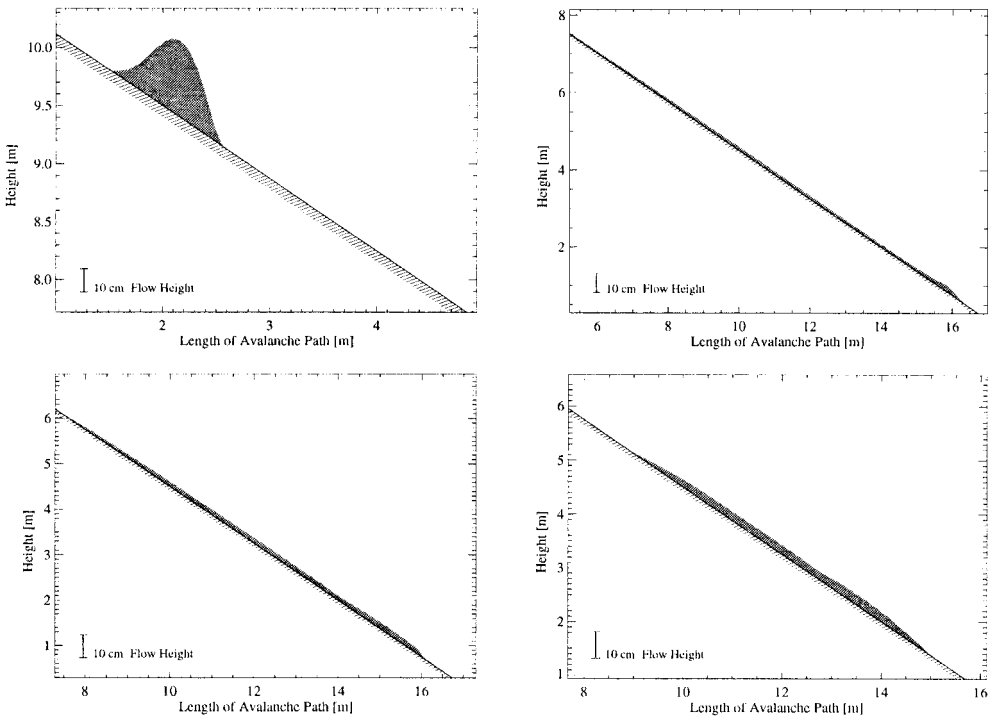

Figure 7. Top left: a parabolic-shaped mass is released from rest. The height is scaled by a factor of 2. Top right: the flow shape with $\phi = 0°$. Note the great length and greater flow heights at the avalanche front. Scaling factor of 5. Bottom left: the flow shape with $\phi = 25°$. Scaling factor of 5. Bottom right: the flow shape with $\phi = 45°$. Note the short length and almost parabolic form. Scaling factor of 5. Bed friction angle $\delta = 22°$ and no viscous friction was specified in all simulations.

A case of practical importance is when the bed friction angle is approximately equal to the terrain slope $\delta \approx \psi$. Often in hazard mapping applications the terrain oscillates between $\delta > \psi$ and $\psi > \delta$. In this case the numerical model predicts that the avalanche will alternately decelerate and accelerate during its downward motion, see Reference [23] for several examples. In the next series of simulations three different bed friction angles $\delta = 31°$, $32°$ and $33°$ were specified for a mass flowing down a slope of $\psi = 32°$. The internal angle of friction remained constant for all three simulations, i.e. $\phi = 30°$. No viscous friction was specified. The mass was released from rest and the initial pile geometry was rectangular ($h_0 = 0.1$ m). Figure 9 shows the position of the avalanche front for the three cases. For $\delta = \psi$ the front position increases linearly in time; for $\delta > \psi$ the mass stops; for $\delta < \psi$ the mass flows rapidly out of the model domain.

The problem with this model behaviour is that for small changes in δ when $\delta \approx \psi$ the model will predict very different runout distances. Note that when $\delta \leq \psi$ the rate of growth of the avalanche length remains linear (Figure 9). Finally, as shown in Figure 10 when $\delta = \psi$ the

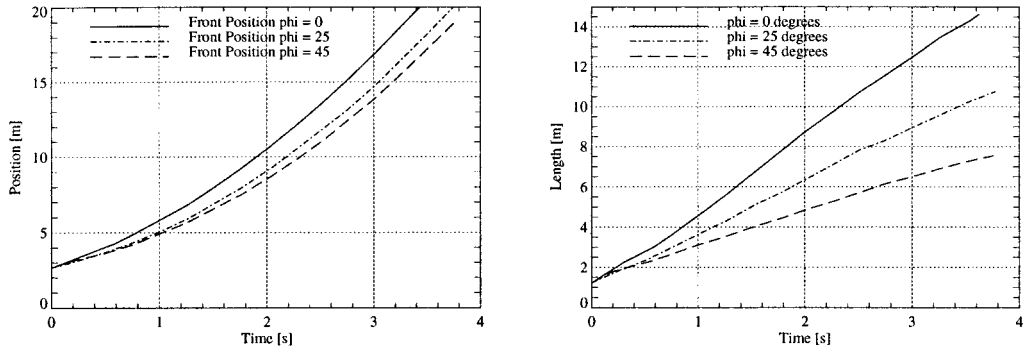

Figure 8. Left: position of avalanche front over time for different internal friction angles ϕ. Right: avalanche length over time. Note the model predicts a near linear increase in length. Internal friction values $\phi = 0°$, 25° and 45°. Bed friction angle $\delta = 22°$. No viscous friction.

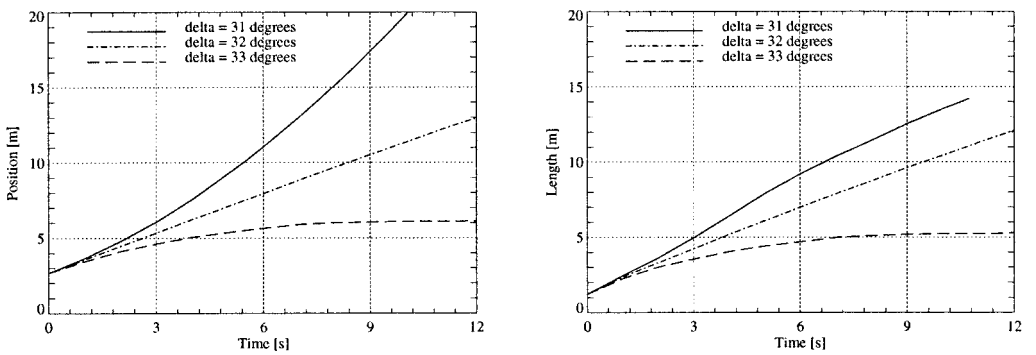

Figure 9. Left: position of avalanche front over time for three bed friction angles ($\delta = 31°$, 32° and 33°). $\psi = 32°$. Right: avalanche length over time. Internal friction angle $\phi = 30°$. No viscous friction. When $\delta \approx \psi$ large differences in simulated front positions occur.

model predicts a long flat avalanche form. The flow heights are nearly constant over the entire length. The rear of the avalanche remains stationary.

In a final series of theoretical simulations the viscous damping term was introduced into the computations, i.e. $1/\xi \neq 0$. The effect of this term on flow behaviour is immediately apparent: the avalanche reaches a steady state flow velocity. This is shown in Figure 11 where two avalanches with and without viscous friction are depicted. In accordance with the Swiss Guidelines we specified $\xi = 3000.0\ \mathrm{m/s^2}$ and $\lambda = 1.0$. Note the large difference in avalanche flow forms.

Finally, no numerical instabilities were encountered during the simulations. Even for the extreme case of a rectangular pile being released from rest with no friction, $\delta = 0°$, $\phi = 0°$ and

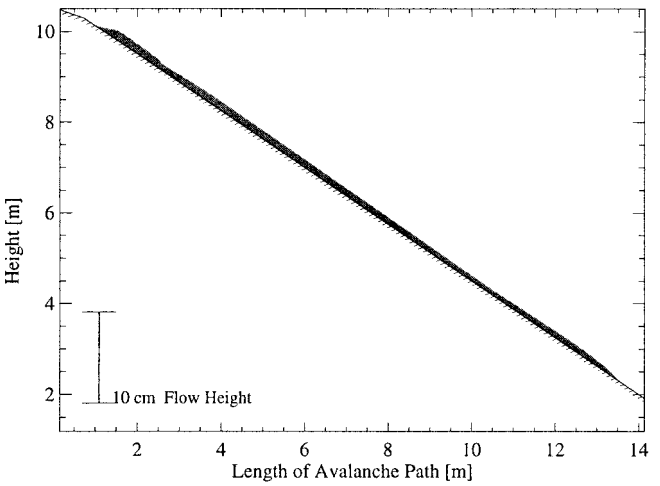

Figure 10. The avalanche shape when $\delta = \psi$. The avalanche rear remains stationary. The avalanche front moves forward with a constant velocity. The flow heights are increased by a factor of 20.

$1/\xi = 0$ the solution schemes remained stable. The predicted avalanche flow form is shown in Figure 12. For comparison the case $\delta = 0°$, $\phi = 30°$ and $1/\xi = 0$ is also displayed.

Well-documented observations of snow avalanche events are rare. For this reason laboratory chute experiments have been carried out to validate granular flow models [5]. Chute experiments have the advantage that the initial fracture conditions, geometry of the avalanche track and properties of the flow materials are well defined. In this section one of the many laboratory experiments published in Reference [5] will be simulated using the first-order model.

The laboratory chute consists of two straight 100 mm wide track segments separated by a short transition zone. In this particular experiment 4 kg of glass beads were released down the first track segment which was inclined at 60° (Experiment 117). The second track segment was flat. The track geometry is shown in Figure 13. The chute was lined with drawing paper to increase the basal friction. The glass beads had a diameter of 3 mm. High speed photography was used to determine the position of the avalanche as a function of time. Complete information, including a series of photographs of the event, can be found in Reference [5].

Figure 13 shows the simulated avalanche at various locations on the track. After release, it accelerates to a terminal velocity of 3.5 m/s before coming to rest on the flat track segment. The calculated runout distance agrees well with the experimental value.

In Figure 14 the calculated and experimental positions of the front, rear and maximum height are displayed. A good agreement exists for both the front and rear positions. The calculated location of the maximum flow height is located nearer to the avalanche front than observed in the experiments. This position is sensitive to the initial conditions, especially the initial form of the mass. In the simulations a rectangular mass with a constant height was released with an initial velocity of 2 m/s. Previous simulations of this experiment use a

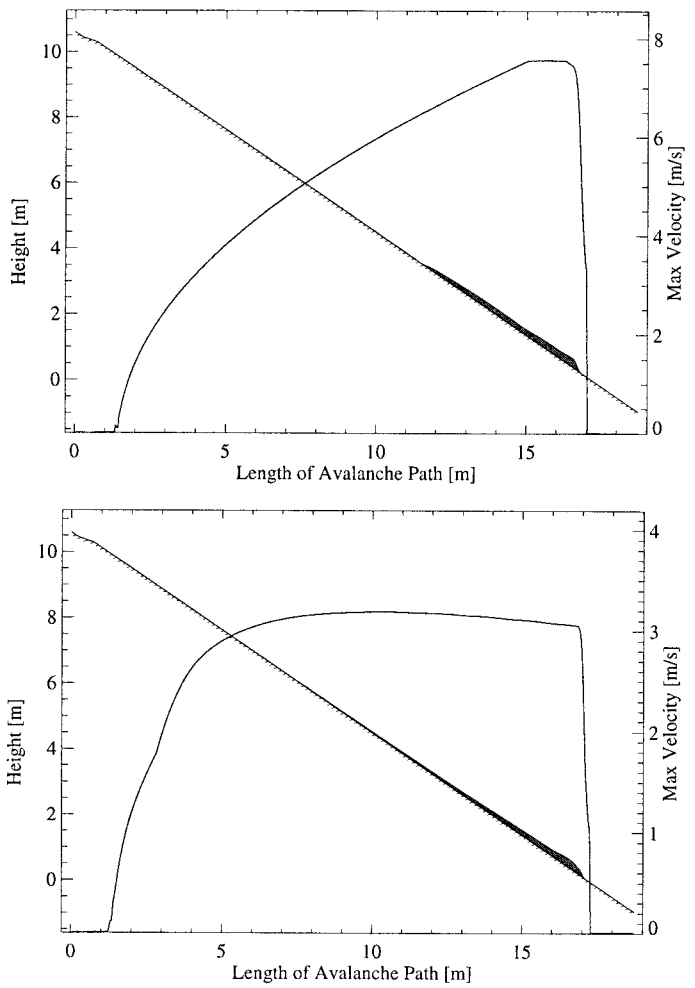

Figure 11. Predicted maximum flow velocities for two avalanches with and without viscous friction. The avalanche with $\xi = 3000\ \mathrm{m/s^2}$ reaches a steady velocity quickly. Note the differences in avalanche shape and length. Slope angle $\psi = 32°$.

Lagrangian finite difference model with artificial diffusion [5]. This model does not employ a turbulent friction to decelerate the flow mass. Instead only a basal Coulomb-type friction and an active/passive internal friction are used. These two friction terms are also employed in our model. In fact, the magnitude of the friction parameters did not differ significantly from those employed in the Lagrangian model ($\mu = 0.49°$ and $\phi = 26°$). However, unlike the Lagrangian model, viscous friction had to be introduced to regulate the flow velocities. Without viscous friction, the avalanche flowed past the end of the chute. A value of $\xi = 2000\ \mathrm{m/s}$ was used in our model.

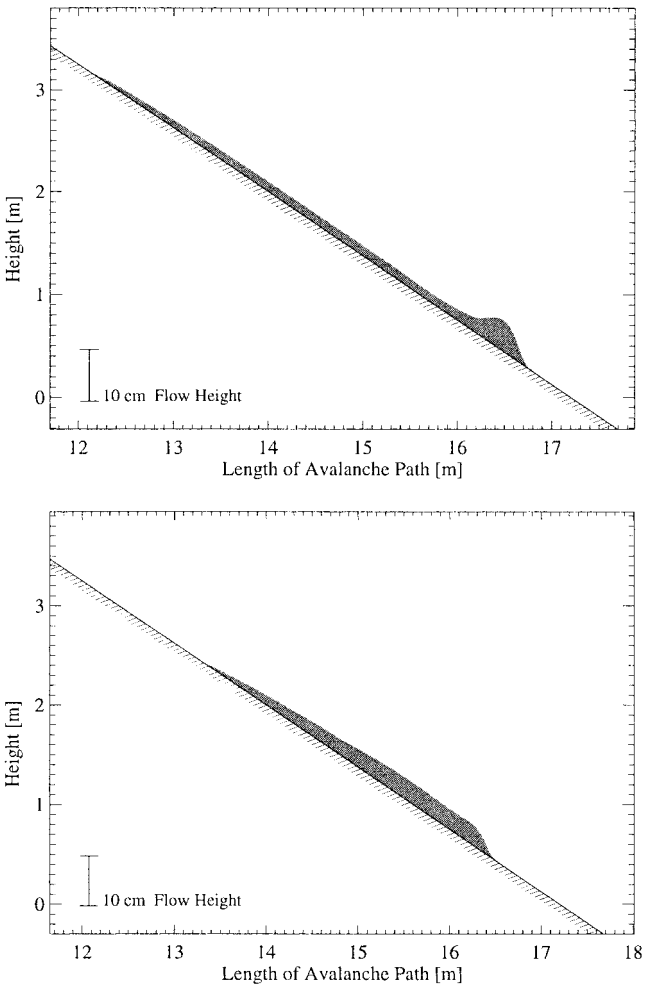

Figure 12. Top: the flow form of an avalanche with no flow friction: $\delta = 0°$, $\phi = 0°$ and $1/\xi = 0$. Bottom: The flow form of an avalanche with: $\delta = 0°$, $\phi = 30°$ and $1/\xi = 0$. The results illustrate the importance of internal friction parameter ϕ. The flow heights are increased by a factor of 5.

The avalanche event used to demonstrate the application of the numerical TVD scheme in practice is one of the four calculation examples of the Swiss Guidelines: the Ariefa avalanche that occurred in early January during the catastrophic avalanche Winter of 1951 in Samedan, Canton Grisons. This avalanche event is often used to test avalanche dynamics models [10,23,24] because the terrain is ideal, see Figure 15. The avalanche profile consists of two track segments of nearly constant slope and width. The transition zone between the avalanche track and runout zone is well defined. Subsequently, the track is suitable for analytical

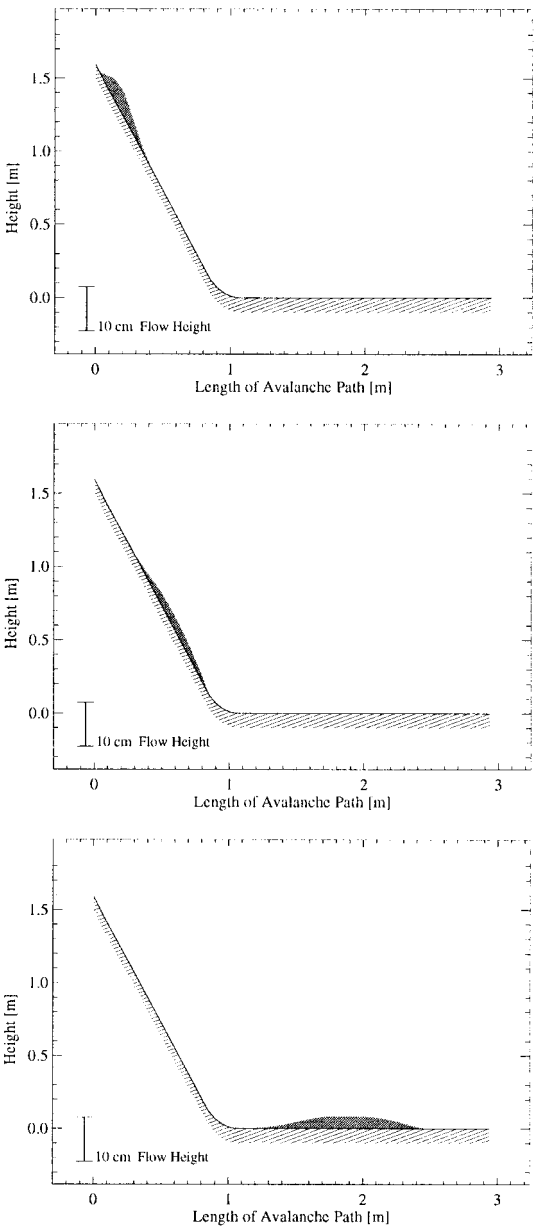

Figure 13. Simulation of a laboratory chute experiment. Four kilograms of glass beads are released down a 60° inclined chute. Top: shortly after release. Middle: in the transition zone. Bottom: At rest position. The flow heights are increased by a factor of 3. The final deposition form agrees well with the experimental results.

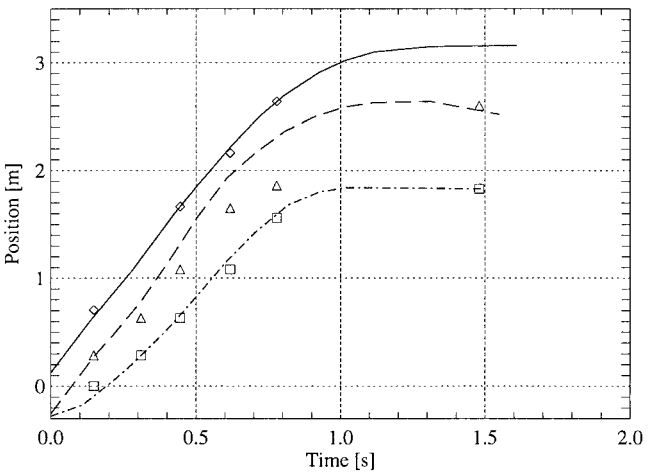

Figure 14. Comparison between measured front (diamonds), rear (squares) and maximum height positions (triangles) and simulation predicted values. The agreement with the front and rear positions is good.

methods and a good first example to test the proposed numerical model. More field examples can be found in Reference [23].

The avalanche fracture zone was large; it extended between 2000 m and 2350 m above sea level and varied in width between 100 m and 180 m. A constant snowpack fracture height of 1 m was specified following the Swiss Guideline recommendations for regional fracture depths, which are statistically related to extreme avalanche return periods. The avalanche fracture volume amounted to over $70000\,\mathrm{m}^3$ of snow. The well calibrated Swiss Guideline friction values, see Reference [3], for extreme avalanche events $\mu = 0.155$ and $\lambda_p = 2.5$ were specified for the simulations. A slightly larger viscous drag coefficient $\xi = 2000\,\mathrm{m/s}^2$ was chosen to offset the smaller (and more realistic flow heights) computed by the numerical model, see Reference [23] for a full explanation. All friction values remained constant, in time and space, for the entire avalanche event. The second-order TVD scheme was employed.

Figure 15 depicts the numerical avalanche at various stages of its motion down the mountain side: (a) in the release zone (the avalanche starts from rest), (b) in the transition zone (the flow heights are over 2 m) and (c) in the runout zone (the avalanche is deposited over a length of 500 m). In each figure the predefined avalanche flow width is shown. The measured runout distance is marked with an arrow; a good agreement between measured and predicted avalanche runout exists. The Swiss Guidelines predict a flow velocity of 26.5 m/s in the transition zone; the TVD scheme 37.0 m/s. The shaded region in the track width profile also shows the predicted high hazard red zone (dynamic pressures greater than 30 kPa) and moderate hazard blue zone (dynamic pressures less than 30 kPa). This information is used by land-use planners when preparing hazard maps. Finally, the model predicts 2.0 m deposition heights which are significantly smaller than the 9.0 m depositions predicted by the Swiss Guidelines.

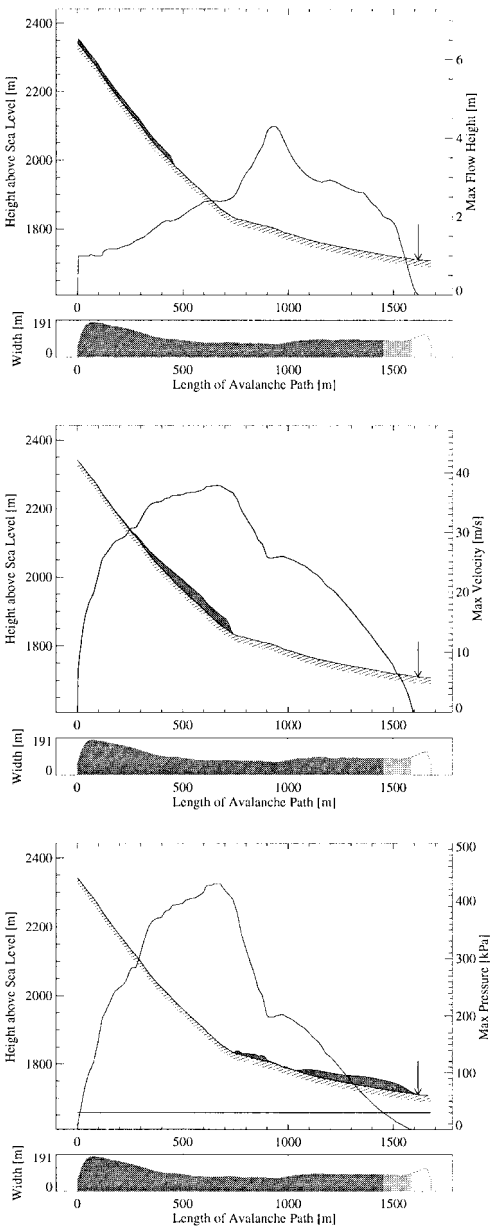

Figure 15. The Ariefa/Samedan avalanche. Top: in the release zone. Predicted avalanche flow heights. Middle: in the transition zone. Bottom: in the runout zone. The middle figure also depicts the maximum flow velocities over the length of the avalanche track. The bottom figure the simulated dynamic impact pressures. The simulated avalanche reaches a terminal velocity of over 30 m/s and traveled over 1.5 km in 60 s. The flow heights are increased by a factor of 15.

6. CONCLUSIONS

In this paper we have presented numerical solutions to the quasi one-dimensional dense snow avalanche modelling problem. The hyperbolic system of equations for the flow height and flow velocity has been discretized using a first-order upwind and a second-order TVD scheme. Although the system may admit discontinuous solutions with shock fronts, solutions to real snow avalanche events are, in general, smooth. Differences in the numerical solutions for the first-order upwind or second-order TVD scheme are therefore minimal; much more important are fluctuations due to the choice of the model's parameters. No artificial viscosity terms have been added to the original equations and the discretized equations only contain parameters that are well known to practitioners of snow avalanche modelling.

Numerical instabilities did not occur even when extreme initial pile geometries (rectangular with steep edges) and flow parameters ($\delta = 0°$, $\phi = 0°$ and $1/\xi = 0$) were specified. The shape of the avalanche flow form depends primarily on the internal friction angle ϕ. For small ϕ values steep and unrealistic avalanche fronts can occur; however, for larger values the avalanche assumes a wedge-like flow form. No M-waves were encountered. The model predicts a linear increase in flow length over time.

Both laboratory chute experiments and avalanche field cases could be simulated. The measured runout distance of the field case could be predicted using friction values near to the values recommended by the Swiss Guidelines on Avalanche Runout Calculation.

This quasi one-dimensional model is now being extended to its equivalent two-dimensional formulation. Here, for geometrical reasons, we use a triangular mesh together with a finite volume approach. The preliminary results, which are now available, are promising and will be presented in the near future.

ACKNOWLEDGMENTS

We would like to thank Dr W. Ammann, head of the Swiss Federal Snow and Avalanche Research (SLF), for his scientific and financial support of the presented research. Dr B. Salm, former head of the avalanche dynamics group of the SLF, and U. Gruber are sincerely thanked for their practical advice. As always Dr O. Buser is thanked for the many fruitful discussions in Zurich and Davos. Finally, we thank the computer support group of the WSL: Dr M. Sonderegger and Dr P. Wielath.

REFERENCES

1. McClung D, Schaerer P. *The Avalanche Handbook*. Mountaineers Books, 1993.
2. Buser O, Frutiger H. Observed maximum runout distances of snow avalanches and the determination of μ and ξ. *Journal of Glaciology* 1980; **26**(94): 121–130.
3. Salm B, Burkard A, Gubler H. Berechnung von Fliesslawinen, eine Anleitung für Praktiker mit Beispielen. In *Mitteilungen des Eidgenössischen Institutes für Schnee und Lawinenforschung*, vol. 47, Davos: Switzerland, 1990.
4. Bartelt P, Salm B. A comparison between steady and transient dense snow avalanche models. In *Proceedings of the Symposium, 60 Years Snow and Avalanche Research*. Davos: Switzerland, 1996.
5. Hutter K, Koch T, Pluess C, Savage S. The dynamics of granular materials from initiation to runout. Part II: experiments. *Acta Mechanica* 1995; **109**: 127–165.
6. Lang R, Leo B. Model of avalanches in three spatial dimensions, comparison to theory and experiments. In *CRREL Report 94–5* 1994.
7. Norem H, Irgens F, Schieldrop B. Simulation of snow-avalanche in runout zones. *Annals of Glaciology* 1989; **13**: 218–225.

8. Hirsch C. *Numerical Computation of Internal and External Flows*, vols. 1 and 2. Wiley: New York, 1990.
9. Savage S, Hutter K. The motion of a finite mass of granular material down a rough incline. *Journal of Fluid Mechanics* 1989; **199**: 177–215.
10. Salm B. Flow, flow transition and runout distances of flowing avalanches. *Annals of Glaciology* 1993; **18**: 221–226.
11. B. Salm, On non-uniform, steady flow of avalanching snow, *International Association of Scientific Hydrology*, *Publ.*, No. 79.
12. Salm B, Gubler H. Measurement and analysis of the motion of dense snow avalanches. *Annals of Glaciology* 1985; **6**: 26–34.
13. Eberle A, Rizzi A, Hirschel EH. *Numerical Solutions of the Euler Equations for Steady Flow Problems*. *Notes on Numerical Fluid Mechanics*. Vieweg, 1993.
14. Dressler R. New non-linear shallow flow equations with curvature. *Journal of Hydraulic Research* 1978; **16**(3): 205–222.
15. Grasso F, Meola C. Euler and Navier–Stokes equations for compressible flows: finite volume methods. In *Handbook of Computational Fluid Mechanics*, Peyret R (ed.). Academic Press: New York, 1996.
16. Taylor ME. *Partial Differential Equations III*. Springer-Verlag: Berlin, 1996.
17. Weiyan T. *Shallow Water Hydrodynamics*. Elsevier Oceanography Series, Water & Power Press: Beijing, 1992.
18. Harten A. High resolution schemes for hyperbolic conservation laws. *Journal of Computational Physics* 1983; **49**: 357–393.
19. Harten A. On a class of high resolution total-variation-stable finite difference schemes. *SIAM Journal on Numerical Analysis* 1984; **21**(1): 1–23.
20. Harten A, Osher S. Uniformly high-order accurate non-oscillatory schemes I. *SIAM Journal on Numerical Analysis* 1987; **24**(2): 27–309.
21. Harten A, Engquist B, Osher S, Chakravarthy S. Uniformly high-order accurate essentially non-oscillatory schemes III. *Journal of Computational Physics* 1987; **71**: 231–303.
22. Harten A. ENO schemes with subcell resolution. *Journal of Computational Physics* 1987; **71**: 231–303.
23. Bartelt P, Gruber U, Salm B. Calculating dense snow avalanche runout using a Voellmy-fluid model with active/passive longitudinal straining. *Journal of Glaciology* 1999; **45**(150): 242–254.
24. McClung D, Mears A. Dry-flowing avalanche runup and runout. *Journal of Glaciology* 1995; **41**(138): 359–372.

